Eur. J. Mineral., 38, 383–396, 2026
https://doi.org/10.5194/ejm-38-383-2026
© Author(s) 2026. This work is distributed under
the Creative Commons Attribution 4.0 License.

European Journal of Mineralogy
Open Access

Boron coordination in haplogranite glasses

Jakob Rauscher[1], Michael Fechtelkord[2], Sandro Jahn[3], Julie A.-S. Michaud[4], Draupadi Mothan[5], Melanie J. Sieber[5,6], Robert B. Trumbull[1], Franziska D. H. Wilke[1], Max Wilke[5], and Bernd Wunder[1]

[1]GFZ Helmholtz Centre for Geosciences, 14473 Potsdam, Germany
[2]Institut für Geologie, Mineralogie und Geophysik, Ruhr-Universität, 44780 Bochum, Germany
[3]Department of Earth and Environmental Sciences, Ludwig-Maximillians-University, 80333 München, Germany
[4]Institute of Earth System Sciences, Leibniz-University, 30167 Hannover, Germany
[5]Institute of Geosciences, University of Potsdam, 14476 Potsdam, Germany
[6]Institute of Applied Geosciences, Technische Universität Berlin, 10587 Berlin, Germany

Correspondence: Robert B. Trumbull (bobby@gfz.de)

Received: 13 November 2025 – Revised: 1 June 2026 – Accepted: 4 June 2026 – Published: 9 July 2026

Abstract. The coordination of boron in silicate melts has been extensively studied in synthetic industrial glasses but rarely in natural volcanic glasses or their synthetic analogues. Because coordination is a controlling factor in the boron isotope exchange between melts and coexisting phases, it is important to close this knowledge gap. We synthesized a set of boron-rich (2 wt % and 5 wt % B_2O_3) haplogranite glasses with water content from 0 wt % to 7 wt % and a variable alumina–alkali ratio, expressed by the aluminum saturation index (ASI), the molar ratio of Al_2O_3 / ($CaO + Na_2O + K_2O$). Boron coordination was determined by ^{11}B MAS-NMR analyses and is expressed as R(IVB), the ratio of tetrahedral (BO_4) to tetrahedral and trigonal (BO_3) groups.

There is a first-order dependency of boron coordination on the ASI ratio within the studied range of 0.8 to 1.7. All glasses with ASI > 1.1 showed nearly exclusive trigonal boron regardless of water and boron concentration. The maximum value of R(IVB) was 7 %. Glasses with lower ASI values showed a steady increase in R(IVB) up to 90 % in a sample with ASI = 0.8. High water contents may favor formation of BO_4 groups as suggested by other glass studies, but there are masking effects related to the quench rates that make this trend inconclusive.

Our results concur with the few existing NMR studies of natural glasses that boron is dominantly in trigonal coordination in peraluminous melts. The trigonal coordination of boron as $B(OH)_3$ in neutral to acidic aqueous fluids means that there should be little if any fractionation of boron isotopes between a granitic melt and exsolved fluid if the granite is peraluminous. For granites with ASI <1.1, the ratio R(IVB) and thus the B-isotope fractionation are expected to strongly increase. We present a predictive model based on ab initio fractionation factors that links $\Delta^{11}B_{melt–fluid}$ with ASI in the melt, which suggests a fractionation of −4 ‰ to −7 ‰ at 730 and 530 °C, respectively, for a granite with ASI = 0.8.

1 Introduction

Studies of boron and its isotopes, ^{11}B and ^{10}B, are widely applied to investigate geologic processes involving aqueous fluids, magmas, and the minerals crystallizing from them, in particular tourmaline (Marschall and Foster, 2018; Trumbull et al., 2022). The success of these applications hinges on knowledge of the B-isotope fractionation among the relevant mineral, fluid, and melt phases, which in turn is controlled by the coordination of boron within them. The boron coordination and isotope fractionation are reasonably well established for minerals and aqueous fluid (Kowalski and Wunder, 2018). However, the case of fluid–melt interaction is more complex because boron coordination in melts varies with the melt composition, and this dependency has not been sufficiently studied to predict B-isotope fractionation in natural systems. That is the aim of the experimental work described herein.

There have been many studies of synthetic borate and borosilicate glasses because of their industrial importance. The review by Aldermann et al. (2025) summarizes the extensive literature on binary borate glasses and the methods used to determine boron coordination. They conclude that trigonal coordination dominates in all but a few binaries (e.g., Te, Bi, Sb) and that ^{11}B MAS-NMR is the method of choice for quantifying coordination. In her review of boro-aluminosilicate glasses, Navrotsky (2002) predicted that boron in silicate melts would be dominantly in trigonal coordination, and this is consistent with NMR analyses of natural rhyolite glasses by Tonarini et al. (2003) and Slejko et al. (2007). Other studies of boro-alumino-silicate glasses (Dingwell et al., 2002; Wu et al., 2011; Schmidt, 2004) noted the importance of the aluminum / alkali ratio on the proportion of trigonal (BO_3) vs. tetrahedral (BO_4) coordination, whereby high Al contents, by forming AlO_4 groups, displace boron from tetrahedral to trigonal coordination. Furthermore, boron and water have an important relationship in melts because boron increases the water solubility, and it also changes the proportion of H_2O and (OH) groups, with the latter favoring formation of BO_4 groups (Dingwell et al., 2002; Schmidt et al., 2004).

In this study, therefore, we determined boron coordination by nuclear magnetic resonance spectroscopy (^{11}B MAS-NMR) in a set of haplogranite glasses with variable water content, a variable alumina / alkali ratio, and variable boron concentration. The implications of our results on boron coordination for predicting the melt–fluid B-isotope fractionation in natural systems are also discussed.

2 Water and boron concentrations and the aluminum / alkali ratio in natural granites

Water concentrations in natural granitic magmas vary depending on the source composition and the degree of fractionation. A key parameter is the water solubility in granitic melts, which depends on pressure but is also enhanced by high concentrations of volatile, "fluxing" elements like fluorine and boron (Holtz et al., 1993; London et al., 2002). Like water, these "flux" elements are concentrated by crystal fractionation, but they also lower the solidus temperature of the melt, thus promoting more fractionation in a positive feedback cycle that allows highly fractionated magmas to maintain high water contents even at low pressure.

The concentration of boron in natural granitic magmas is hard to determine from the study of rocks because there are significant losses of boron by volcanic degassing and volatile release from crystallizing plutons. Typical whole-rock values of B_2O_3 in granites and rhyolites reach tens to low hundreds of ppm (London et al., 2002; Tonarini et al., 2003; Trumbull and Slack, 2018), which are minimum estimates for the original, magmatic concentration. Melt inclusions in magmatic quartz from volcanic rhyolite, which represent non-degassed magma, can have several hundred ppm B (Lehmann et al., 2000; Schmitt and Simon, 2004). Solubility experiments suggest that the presence of tourmaline in granites implies percent-level concentrations of B in the magma (Wolf and London, 1997; London, 2011), while analysis of melt inclusions in highly evolved granites and pegmatites confirms levels of B in the thousands of ppm (Thomas et al., 2003; Zajacz et al., 2008; Pichavant et al., 2024).

The alkali / alumina ratio is commonly expressed by the alumina saturation index or ASI, which is calculated as the molar ratio Al_2O_3 / ($CaO + Na_2O + K_2O$); see Acosta-Vigil et al. (2003). Based on the ASI value, granites are classified as peraluminous (ASI >1), metaluminous (ASI $=1$), and peralkaline (ASI <1). The majority of granitic magmas making up the continental crust – indeed the bulk crust itself – are metaluminous, having about the same proportion of alkali elements and aluminum as the feldspar minerals. Peralkaline granites, with an overabundance of alkalis compared to feldspars, are relatively uncommon. They typically occur in continental rift settings and are thought to form from extensive fractionation of alkaline basalts. Although generally poor in boron, some examples of peralkaline granites and related pegmatites with borosilicate minerals including tourmaline have been described (Filip et al., 2012; Sunde et al., 2020; De la Cruz et al., 2024).

The peraluminous granites are a widespread group, being found mostly in orogenic settings with thick continental crust where mid-crustal temperatures were high enough to cause partial melting of former sedimentary rocks that were enriched in alumina due to surficial weathering and formation of clay minerals. Granitic magmas formed in this way have relatively high contents of volatile elements (water, F, Li, B), and there is a close global association of peraluminous granites with mineralized pegmatites and magmatic–hydrothermal ore deposits of Sn, W, Li, U, Nb, and Ta (Barton, 1996; Cuney, 2014; Romer and Kroner, 2016; Lehmann, 2021). These granites and associated ores are commonly rich in boron and contain tourmaline group minerals, which is why they have long been a focus of B-isotope studies aimed at understanding fluid–rock interaction and ore formation (Smith and Yardley, 1996; Codeço et al., 2017; Trumbull and Slack, 2018; Trumbull et al., 2020; Zhao et al., 2022; Sun et al., 2024).

3 Experimental design and methods

3.1 Synthesis of starting materials

A starting glass with the target composition of water-free haplogranite (normative $Ab_{40}Or_{25}Qz_{35}$) was prepared from powdered, reagent-grade SiO_2, Al_2O_3, Na_2CO_3, and K_2CO_3. The strongly hydrophilic Al_2O_3 powder was heated before use at one atmosphere at 800 °C for 3 h to remove any moisture. The reagents were thoroughly mixed and held at 1600 °C in an open platinum crucible for 2 d to drive off

CO_2 and anneal the melt. The crucible was quenched in a water bath, and the resulting glass was then crushed to powder in an agate mortar and remelted at 1600 °C for 4 d. The bubble-free glass was then re-crushed and stored in a vacuum desiccator.

The starting glass has a nominal ASI value (molar Al_2O_3 / ($CaO + Na_2O + K_2O$)) of 1.0 (see Rauscher et al., 2026, for glass analyses). From aliquots of the powdered and twice-homogenized starting glass, we prepared two other mixtures with nominal ASI values of 0.7 and 1.3 by adding appropriate amounts of Al_2O_3, Na_2CO_3, and K_2CO_3. These were fused and ground to powder twice in the same way as with the starting glass. From each of the anhydrous glass powders with nominal ASI values of 0.7, 1.0, and 1.3, we prepared hydrous, boron-bearing glasses in the following way: the glass powder was mixed with reagent-grade boric acid and loaded into platinum capsules (5 mm diameter, 25 mm length, ca. 50 mg powder) with doubly distilled water in sufficient quantity to achieve nominal concentrations of 2 wt % or 5 wt % B_2O_3 and 4 wt % or 6 wt % H_2O. The water-bearing capsules were welded shut and held for 3 d in internally heated pressure vessels (IHPVs) at 300 MPa and 1100 °C in laboratories of the GFZ Potsdam or the Institute of Earth System Sciences, Leibniz University Hannover. The accuracies in temperature and pressure at both institutes were around ±10 °C and ±5 MPa, respectively. After cold pre-compression with Ar, samples were heated to 1100° at a rate of ∼ 30 °C min^{-1}. Pressure increased during heating until reaching the target value or was adjusted if necessary. The oxygen fugacity (fO_2) was intrinsically buffered by the IHPV, yielding a log $fO_2 \sim +2.8$ relative to the nickel–nickel oxide buffer (NNO) for water-saturated samples. The samples were quenched by turning off the heating power. Subsequently, the capsules were checked for signs of leakage and weighed; weight loss or capsule failure were grounds for rejection.

The water-free glasses with nominal 2 wt % and 5 wt % B_2O_3 were prepared in a similar way, but the platinum capsules were crimped shut and not welded, then heated at one atmosphere to 1600 °C for 3 d and left for 3 h at 1100 °C before quenching in a water bath. The quenched glass beads recovered from the capsules were washed in doubly distilled water, dried, and cut in half. One half was mounted in epoxy resin for optical examination and analysis by electron microprobe and Raman spectroscopy, while the other half was ground to powder in an agate mortar for use in NMR analysis. The electron microprobe work was done after a first session of NMR analyses, and it revealed a preparation error such that the six samples with nominal ASI = 0.7 in fact had ASI close to 1.1. Six new glasses were made with the correct mixtures, and in addition, we prepared duplicate aliquots of four samples whose NMR results in the first session appeared anomalous. In total, 29 samples were analyzed by NMR in the two sessions.

3.2 Electron microprobe analysis

The polished epoxy mounts with glass samples were carbon-coated and analyzed at the GFZ microanalytical laboratories using a field-emission microprobe JEOL JXA8530F+ instrument fitted with five wavelength-dispersive spectrometers. The microprobe was operated at 10 kV and 40 nA, with a beam size of 20 µm, resulting in a current density of 0.013 nA mm^{-2}, for which negligible loss of sodium is expected (Morgan and London, 2005). Peak measurement times were 50 s for boron and 10 s for all other elements. The most volatile elements, boron and sodium, were measured first and simultaneously. The X-ray peak, calibration standard, and crystals used were as follows – B–Kα (schorl, LDEB), K–Kα (orthoclase, PETL), Fe–Kα (schorl, LiFL), Na–Kα (albite, TAPL), Al–Kα (albite, TAPL), Si–Kα (albite, PETH), and P–Kα (apatite, PETH). The LDEB multilayer Mo / B_4C crystal produces boron X-ray fluorescence, which can bias results, especially for low-concentration samples. We used the calibration-curve procedure of Wilke (2023) to correct for this effect, adjusting the measured values downward by between 0.4 wt % and 0.6 wt %. The microprobe results are summarized in Table 1, and all data are reported in the data supplement (Rauscher et al., 2026).

3.3 Raman spectroscopy

The polished glass samples (same mounts as for EPMA) were analyzed for H_2O content in situ using a Raman LabRAM HR 800 spectrometer (HORIBA Jobin Yvon) equipped with a 532 nm air-cooled Nd : YAG laser, a Peltier-cooled multichannel CCD detector (1024 pixel), a high-precision motorized xy translation stage for Raman confocal mapping, and a confocal microscope BX41 (Olympus) with white light illumination for observation in transmitted and reflected mode. A grating of 300 was used along with a 100× objective. The spectra were recorded from 100 to 4000 cm^{-1} to include both the alumino-silicate (100 to 1350 cm^{-1}) and the OH (2900 to 3800 cm^{-1}) regions. The spectrometer was calibrated beforehand to the Si peak at 521 cm^{-1}. A rhyolitic hydrous glass with known water content of 4.2 ± 0.6 wt % H_2O by Spallanzani et al. (2022) was used as a reference sample (LPR200). Line measurements with 6 to 15 spots, depending on sample size, were conducted across the samples with an acquisition time of 5 s with five accumulations per spot. The water content was quantified using the procedure described by Schiavi et al. (2018) for rhyolitic glasses using the intensity of the OH stretching bands between 3000 and 3800 cm^{-1}. The baseline was subtracted from the spectra using the anchor points reported in Schiavi et al. (2018) and Spallanzani et al. (2022). The area A3550 of the OH stretching mode between 2980 and 3780 cm^{-1} was normalized to the area A500 of the alumino-silicate region at ca. 500 cm^{-1} (T–O–T bending modes), between 190 and 1250 cm^{-1}. The water content was obtained by multi-

https://doi.org/10.5194/ejm-38-383-2026

Table 1. Chemical composition of experimental glasses by electron microprobe analysis (EPMA) and Raman spectroscopy, in weight percent.

Sample Number	n	$B_2O_3^*$ wt %	SD	SiO_2 wt %	SD	Al_2O_3 wt %	SD	K_2O wt %	SD	Na_2O wt %	SD	Subtotal wt %	H_2O (diff.)	H_2O (Raman)	SD	TOTAL	ASI	SD
R2	20	1.93	0.27	77.1	0.58	12.1	0.07	3.69	0.06	3.76	0.07	98.5	1.47	0	0.6	98.5	1.19	0.02
K2	15	2.69	0.49	71.6	0.31	10.8	0.05	3.3	0.08	3.76	0.04	92.1	7.91	7.1	1.3	99.2	1.11	0.02
P3	20	1.47	0.58	78.6	1.1	11.8	0.07	3.3	0.07	3.46	0.04	98.7	1.32	ND		*100*	1.28	0.02
L1	15	4.9	0.59	70.1	0.35	10.5	0.05	3.18	0.03	3.62	0.04	92.3	7.65	7.24	1.3	99.6	1.12	0.01
M1	15	5.12	0.51	71.1	0.35	10.7	0.05	3.64	0.03	3.94	0.05	94.5	5.53	4.58	0.8	99.1	1.03	0.01
Q1	15	1.78	0.3	77.4	0.35	11.6	0.06	3.57	0.03	3.85	0.03	98.2	1.8	0	0.6	100	1.14	0.01
A3	14	1.99	0.53	70.9	0.5	10.6	0.05	3.32	0.04	3.35	0.05	90.1	9.86	6.77	1.3	96.9	1.16	0.02
B3	15	2.14	0.38	73.2	0.38	11.1	0.06	3.2	0.03	3.49	0.06	93.1	6.93	4.61	0.8	97.7	1.2	0.01
S1	15	3.85	0.8	75.1	0.52	11.3	0.1	3.47	0.04	3.66	0.04	97.4	2.63	0.19	0.6	97.6	1.16	0.01
C3	15	4.83	0.33	70.3	0.71	10.3	0.06	3.27	0.03	3.27	0.1	91.9	8.06	4.72	0.9	96.7	1.15	0.02
D4	15	5.19	0.26	71.1	0.43	10.5	0.05	3.37	0.03	3.51	0.03	93.7	6.31	7.44	1.4	101.1	1.11	0.01
N1	15	1.77	0.62	74.1	0.54	13.9	0.08	3.54	0.03	3.83	0.04	97.2	2.84	ND		*100*	1.37	0.01
N2	16	1.99	0.62	74.1	0.39	13.8	0.06	3.56	0.04	3.81	0.31	97.3	2.67	0.1	0.6	97.4	1.37	0.09
E13	15	1.83	0.65	70.6	0.59	15.6	0.59	3.53	0.05	3.65	0.06	95.3	4.7	2.91	0.6	98.2	1.59	0.08
F3	19	2.83	0.23	70.8	0.23	14.6	0.08	3.4	0.04	3.37	0.03	95	5.03	ND		*100*	1.58	0.01
O2	15	4.73	0.5	72	0.37	13.4	0.06	3.44	0.04	3.76	0.03	97.3	2.65	ND		*100*	1.36	0.01
H3	15	5.12	0.48	67.5	0.54	15	0.39	3.03	0.04	3.29	0.06	93.9	6.08	4.57	0.8	98.5	1.72	0.07
G2	15	4.93	1.2	72.1	1.13	13.7	0.13	3.39	0.06	3.79	0.05	97.9	2.09	0	0.6	98.5	1.39	0.02
P4	15	1.6	0.45	75.5	0.43	11.8	0.05	4.84	0.04	5.43	0.06	99.2	0.8	0	0.6	99.2	0.83	0.01
J3	15	1.71	0.38	72.9	0.48	11	0.06	4.95	0.04	5.03	0.03	95.6	4.37	3.16	0.6	98.8	0.81	0
J11	15	1.57	0.55	72.9	0.35	11.3	0.04	4.68	0.04	5	0.03	95.4	4.55	4.01	0.7	99.5	0.85	0
K3	15	2.07	0.38	72.4	0.38	10.8	0.07	4	0.03	4.05	0.04	93.4	6.63	3.96	0.7	97.3	0.99	0.01
R3	15	4.64	0.52	73.7	0.39	11.4	0.05	4.63	0.03	5.24	0.04	99.6	0.42	ND		*100*	0.84	0.01
L2	11	5.07	0.68	70.4	0.44	10.9	0.04	4.53	0.03	4.85	0.04	95.7	4.27	4.58	0.8	100.3	0.85	0.01
M2	15	4.76	0.42	72.1	0.43	11.2	0.03	4.38	0.02	4.95	0.06	97.4	2.59	0	0.6	98.01	0.87	0.01

Mean and standard deviation of "n" analyses (for EPMA). Number of Raman spectra from each sample is between 6 and 15. All data are provided in Rauscher et al. (2026). Total values listed with decimals are based on H_2O from Raman analyses, and values of 100 in italics are based on H_2O by difference. $*$ B_2O_3 by EPMA is adjusted for X-ray fluorescence of the LDEP crystal after Wilke (2023). H_2O by difference is (100 – EPMA subtotal). H_2O by Raman spectroscopy; see data supplement Table 2. ND – not determined. ASI: molar ratio Al_2O_3 / ($Na_2O + K_2O$).

plying the ratio A3550 / A500 by the calibration coefficient obtained on the reference glass. The H_2O values are reported in Table 1, where the uncertainties include counting statistics on sample and reference glass as well as the uncertainty in the H_2O content of the reference glass. All data from the samples and reference glass are reported in the data supplement (Rauscher et al., 2026). The standard deviation of H_2O contents from spectra 6 to 15 for each sample was smaller than the uncertainty (data supplement), indicating a homogeneous distribution of H_2O in the samples.

3.4 Nuclear magnetic resonance analysis

The coordination of boron in glasses was determined by ^{11}B MAS-NMR spectroscopy (magic angle spinning nuclear magnetic resonance) at the Ruhr-Universität Bochum in the Geoscience Solid State NMR Spectrometry Facility. The analyses were performed on a Bruker AVANCE NEO 400 NMR spectrometer (9.34 T). Measurements were made on powdered samples at a frequency of 128.44 MHz with a CPMAS H/X WVT double-resonance probe head at a spinning rate of 12.5 kHz. For the ^{11}B MAS-NMR experiments, a short single-pulse duration of 0.6 µs (100 W) was used to ensure homogenous excitation of the central and all satellite transitions. A recycle delay of 1 s was used for the accumulation of 3200 scans. Typically, about 40–60 mg of materials was transferred and packed into a zirconia rotor and sealed with a DELRIN turbine cap. Solid $NaBH_4$ was used as a secondary reference standard ($\delta_{iso} = -42.0$ ppm for $NaBH_4$), measured separately. The ^{11}B MAS-NMR spectra were fitted with quadrupolar or Gaussian/Lorentzian line shapes including convolution using the DmFit 2010 program (Massiot et al., 2002). Tolerances were estimated by varying the parameters in the fit function until a distinct change in χ^2 took place. The relative proportions of the BO_3 and BO_4 species were determined from the respective area ratios. The error in area ratios is between 2 % and 5 % depending on the signals. An illustration of the peak fitting is shown in Fig. 1 for sample R3, which has a mixed boron coordination, with 66 % in BO_3 and 34 % in BO_4 groups. After the initial session of NMR analyses, repeat analyses of samples K2, P3, L1, and M1 (aliquots of the same glass powder) were made to confirm results that appeared anomalous. In all cases, the repeat analyses ("R" in the sample number) showed good agreement with the originals (Table 2), and this comparison also gives a measure of the NMR repeatability.

4 Results

The chemical compositions of 25 experimental glasses derived from multiple microprobe analyses of epoxy-mounted glass beads are summarized in Table 1, which gives a mean value and standard deviation of 10 to 20 analyses per sample. The results demonstrate good homogeneity of each glass (see also data supplement in Rauscher et al., 2026).

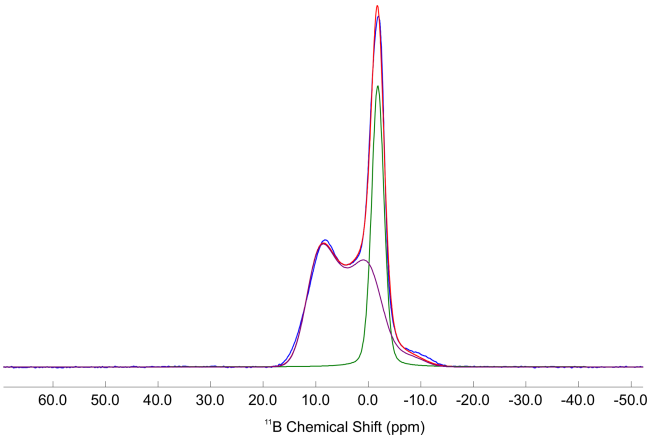

Figure 1. Example of peak fitting the ^{11}B MAS-NMR spectrum of sample R3, showing the experimental signal (blue), overall theoretical signal (red), quadrupolar line shape of trigonal boron (purple), and Gaussian/Lorentzian line shape of tetrahedral boron (green). The ratio of BO_3 to BO_4 in this sample is 66 : 34 (Table 2).

The results of ^{11}B MAS-NMR analysis on 29 samples (25 glasses and 4 repeat analyses) are shown in Table 2, which lists the integrated areas and amplitudes of the BO_3 and BO_4 resonance peaks, with values of isotropic chemical shift, quadrupolar coupling (C_Q), and asymmetry parameter (η). Two exemplary spectra are shown in Fig. 2 for glasses with dominantly tetrahedral and trigonal boron. The main features of the ^{11}B MAS-NMR spectra are a broad pattern caused by second-order quadrupolar interaction related to trigonal planar BO_3 groups (IIIB) and a symmetric, Gaussian resonance pattern centered around 0 ppm that corresponds to tetrahedral BO_4 groups (IVB). Overall, the proportion of IVB varies from 0 % to 92 %. A striking feature of the data is that all samples with ASI > 1.1 have less than 10 % tetrahedral-coordinated boron, whereas the IVB proportion increases to 20 % and more for samples with ASI near 1.0 and continues to rise as ASI decreases to the minimum value in this study at 0.81.

Figures 3 to 5 illustrate the complexity of relationships between boron coordination as expressed by the ratio $R(\mathrm{IVB}) = \mathrm{IVB} / (\mathrm{IVB} + \mathrm{IIIB})$ and the chemical composition of the glasses. The first-order dependency of boron coordination is on the alumina / alkali ratio. All glasses with ASI > 1.1 essentially have no tetrahedral boron regardless of their water content (Fig. 3) and their boron concentration (Fig. 4).

Figure 5 illustrates a feature of the relationship between alkali content and B coordination in glass that is known from studies of industrial glasses (see discussion). The plot shows total alkali concentration in wt % oxide against the concentration of tetrahedral-coordinated boron as wt % B_2O_3 (calculated from the R(IVB) ratio from NMR and wt % total B_2O_3 from EPMA). There is negligible tetrahedral boron for all alkali concentrations below 7.5 wt % (i.e., samples with

Table 2. Results of ^{11}B MAS-NMR analysis of experimental glasses.

Sample	Peak	Shift. (ppm)	C_Q (kHz)	η	Peak integral	Peak amplitude	Boron coordination	R(IVB)
R2	1	n/a	n/a	n/a	n/a	n/a	n/a	0.0
	2	14.0	2646	0.18	3.06E+09	3.90E+06	trigonal	100.0
K2	1	−1.2	n/a	n/a	2.70E+09	6.69E+06	tetrahedral	54.2
	2	16.4	2568	0.22	2.28E+09	3.09E+06	trigonal	45.8
K2R	1	−1.2	n/a	n/a	2.95E+09	7.24E+06	tetrahedral	55.2
	2	16.3	2532	0.00	2.40E+09	3.34E+06	trigonal	44.8
P3	1	−1.7	n/a	n/a	6.47E+08	1.26E+06	tetrahedral	6.7
	2	14.0	2625	0.12	9.04E+09	1.17E+07	trigonal	93.3
P3R	1	−1.6	n/a	n/a	8.72E+08	1.92E+06	tetrahedral	7.6
	2	13.9	2614	0.00	1.06E+10	1.38E+07	trigonal	92.4
L1	1	−0.6	n/a	n/a	2.62E+09	6.74E+06	tetrahedral	20.7
	2	16.6	2649	0.16	1.00E+10	1.28E+07	trigonal	79.3
L1R	1	−0.7	n/a	n/a	3.05E+09	7.80E+06	tetrahedral	21.1
	2	16.6	2656	0.16	1.14E+10	1.45E+07	trigonal	78.9
M1	1	1.1	1129	0.45	2.44E+09	1.71E+07	tetrahedral	19.6
	2	16.1	2633	0.18	1.00E+10	1.29E+07	trigonal	80.4
M1R	1	−0.8	n/a	n/a	3.40E+09	8.02E+06	tetrahedral	23.4
	2	16.2	2610	0.19	1.11E+10	1.46E+07	trigonal	76.6
Q1	1	n/a	n/a	n/a	n/a	n/a	n/a	0.0
	2	14.1	2649	0.25	4.64E+10	5.91E+07	trigonal	100.0
A3	1	1.0	894	0.57	4.53E+09	5.05E+07	tetrahedral	2.7
	2	15.8	2585	0.09	1.62E+11	2.16E+08	trigonal	97.3
B3	1	1.1	1135	0.35	6.63E+09	4.60E+07	tetrahedral	4.3
	2	15.5	2569	0.15	1.47E+11	1.99E+08	trigonal	95.7
S1	1	n/a	n/a	n/a	n/a	n/a	n/a	0.0
	2	13.9	2628	0.25	1.53E+11	1.98E+08	trigonal	100.0
C3	1	0.5	1055	0.50	2.40E+09	1.93E+07	tetrahedral	3.9
	2	15.6	2603	0.19	5.89E+10	7.76E+07	trigonal	96.1
D4	1	0.6	1066	0.48	2.95E+09	2.32E+07	tetrahedral	4.7
	2	16.0	2576	0.18	5.93E+10	7.99E+07	trigonal	95.3
N1	1	n/a	n/a	n/a	n/a	n/a	n/a	0.0
	2	13.7	2609	0.00	5.26E+10	6.91E+07	trigonal	100.0
N2	1	n/a	n/a	n/a	n/a	n/a	n/a	0.0
	2	13.6	2607	0.00	5.63E+10	7.40E+07	trigonal	100.0
E13	1	n/a	n/a	n/a	n/a	n/a	n/a	0.0
	2	15.6	2617	0.12	4.78E+09	6.24E+06	trigonal	100.0
F3	1	n/a	n/a	n/a	n/a	n/a	n/a	0.0
	2	16.4	2645	0.27	4.89E+09	6.25E+06	trigonal	100.0
O2	1	n/a	n/a	n/a	n/a	n/a	n/a	0.0
	2	14.1	2640	0.24	1.13E+11	1.45E+08	trigonal	100.0

Table 2. Continued.

Sample	Peak	Shift. (ppm)	C_Q (kHz)	η	Peak integral	Peak amplitude	Boron coordination	R(IVB)
H3	1	n/a	n/a	n/a	n/a	n/a	n/a	0.0
	2	15.5	2616	0.10	1.14E+10	1.49E+07	trigonal	100.0
G2	1	n/a	n/a	n/a	n/a	n/a	n/a	0.0
	2	14.3	2641	0.25	1.04E+10	1.34E+07	trigonal	100.0
P4	1	−2.0	n/a	n/a	2.21E+09	6.09E+06	tetrahedral	46.3
	2	14.1	2577	0.00	2.56E+09	3.44E+06	trigonal	53.7
J3	1	−1.6	n/a	n/a	5.03E+09	1.31E+07	tetrahedral	89.8
	2	14.6	2551	0.00	5.73E+08	1.01E+06	trigonal	10.2
J11	1	−1.4	n/a	n/a	4.93E+09	1.25E+07	tetrahedral	91.1
	2	15.0	2271	0.00	4.83E+08	8.37E+05	trigonal	8.9
K3	1	−1.3	n/a	n/a	4.91E+09	1.26E+07	tetrahedral	87.3
	2	16.0	2664	0.00	7.15E+08	9.00E+05	trigonal	12.7
R3	1	−1.8	n/a	n/a	4.16E+09	1.01E+07	tetrahedral	33.8
	2	14.1	2546	0.00	8.14E+09	1.12E+07	trigonal	66.2
L2	1	−1.1	n/a	n/a	6.12E+09	1.38E+07	tetrahedral	48.6
	2	16.1	2472	0.20	6.47E+09	9.46E+06	trigonal	51.4
M2	1	−0.9	n/a	n/a	6.13E+09	1.42E+07	tetrahedral	45.3
	2	16.5	2518	0.18	7.40E+09	1.04E+07	trigonal	54.7

Shift – isotropic chemical shift (ppm). C_Q – quadrupolar coupling constant. η – asymmetry parameter. n/a: not applicable.

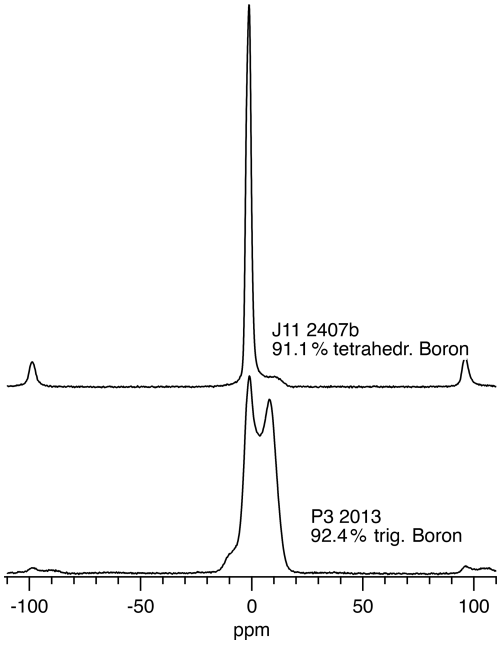

Figure 2. Examples of NMR spectra. The symmetric IVB peak dominates the spectrum for sample J11 (top), while sample P3 (bottom) shows the characteristic doublet of IIIB.

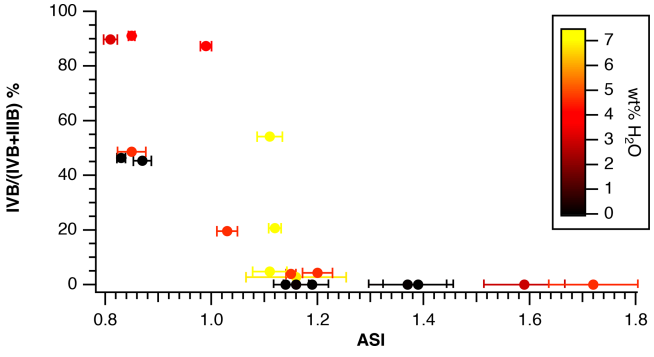

Figure 3. Proportion of tetrahedral boron $R(\mathrm{IVB}) = \mathrm{IVB} / (\mathrm{IVB} + \mathrm{IIIB})$ to ASI (molar $Al_2O_3 / Na_2O + K_2O$) with water contents represented by symbol colors (Raman analysis). The error bars on ASI are from Table 1. Five samples lacking Raman data are not plotted.

ASI > 1.1), a steady increase to a maximum of about 2.5 wt % IVB at 9 wt % to 9.5 wt % alkali oxide, and a decline in tetrahedral boron at high alkali concentrations. This pattern is discussed more fully below.

The coordination of boron in synthetic borate and borosilicate glasses has been extensively studied since the 1980s using ^{11}B MAS-NMR and Raman spectroscopy, which establish general features of boron coordination as a function

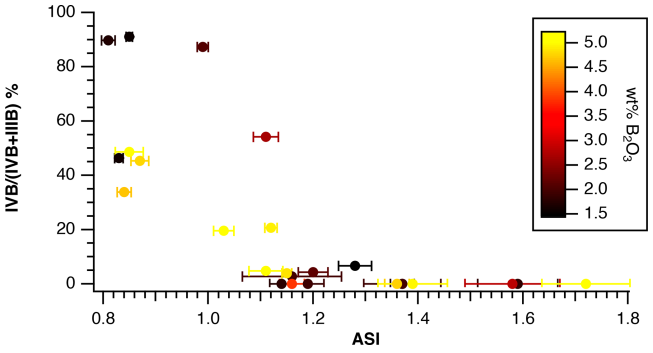

Figure 4. Proportion of tetrahedral boron $R(\mathrm{IVB}) = \mathrm{IVB} / (\mathrm{IVB} + \mathrm{IIIB})$ to ASI (molar $Al_2O_3 / CaO + Na_2O + K_2O$), with boron contents represented by symbol colors. The error bars on ASI are from Table 1. Symbol colors represent total boron content.

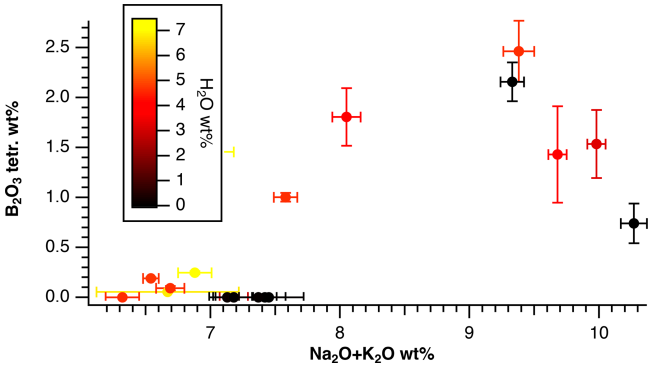

Figure 5. Weight percent boron in tetrahedral coordination against total alkali concentration in wt %, with water contents represented by symbol colors (Raman analysis). The error bars are from Table 1. Five samples lacking Raman data are not plotted. Note the drop in IVB above 9.3 wt % alkalis.

of composition (e.g., Bray and O'Keefe, 1963; Bray, 1985; Stebbins and Ellsworth, 1996; Wu and Stebbins, 2010). The glass compositions in these studies are rarely close to those of melts in nature, and we are aware of just two experimental NMR studies in natural samples, both conducted on rhyolite glasses with peraluminous composition from Italy. Tonarini et al. (2003) studied rhyolites from three different localities with ASI = 1.1 to 1.3 and found that all had dominantly (76 % to 92 %) trigonal boron coordination. Slejko et al. (2007) conducted NMR analyses of a rhyolite glass with ASI = 1.1 and found a proportion of 75 % trigonal boron.

4.1 Variations in R(IVB) with alumina / alkali ratio

The boron coordination is strongly dependent on the ratio of network-forming and network-modifying cations in the melt. Considering the reaction of trigonal to tetrahedral boron groups, where NBO denotes a non-bridging oxygen,

$$BO_4 \leftrightarrow BO_3 + \mathrm{NBO}, \quad (1)$$

it is clear that a conversion of boron from trigonal to tetrahedral groups depends on the availability of NBO and thus on the concentration of network-modifying cations (alkalis, alkaline earths). Importantly, however, alkali oxides also promote formation of AlO_4 in melts, and studies of alkali–aluminosilicate glass have shown that high Al contents reduce the proportion of BO_4 by competing for the available alkalis (Wu and Stebbins, 2010). Therefore, the ASI parameter is a key variable. The influence of ASI on B coordination is shown by our results (Table 2, Figs. 3 and 4), where all compositions with ASI > 1.1 show low to negligible proportions of BO_4, while for the others, the proportion of BO_4 increases systematically with falling ASI. For strongly peraluminous compositions with ASI > 1.1, it appears that all available alkalis are utilized to stabilize AlO_4, and therefore all boron is in trigonal coordination. It follows from Eq. (1) that competition for NBOs with network-modifying cations (alkalis, alkaline earths) will determine the maximum proportion of BO_4 reachable for a given composition. The study of borate glasses by Bray and O'Keefe (1963) showed that the addition of alkalis increased the proportion of BO_4 up to a maximum at 30 mol % to 40 mol % of alkali oxide, after which the BO_4 proportion fell to near zero at 70 mol % alkali oxide. This so-called "boron anomaly" was also found in borosilicate glasses (e.g., Scholze 1988). Although the addition of aluminum and water complicates the relationship of the alkali–boron ratio to boron coordination referred to in the works cited, the observation shown in Fig. 5 suggests that a phenomenon like the boron anomaly is present in hydrous, aluminosilicate glasses as well.

4.2 Variations in R(IVB) with water concentration

It is well known that the addition of water to boron-rich melts leads to formation of OH groups in the melt, which have a similar network-modifying role to alkalis and a similar lowering effect on melt viscosity (Hess et al., 1995; Schulze et al., 1996). In principle, then, higher water content should enhance the formation of BO_4 groups, and this was observed by Schmidt et al. (2004) in dry vs. hydrated albite glass, although the difference in their study was small (2 % vs. 6 % tetrahedral boron, respectively, for 0 wt % vs. 4.4 wt % H_2O). Our results show no clear correlation of the R(IVB) ratio with water concentration overall (trigonal coordination prevails in peraluminous glasses regardless of H_2O content), but there is a tendency to higher R(IVB) in hydrous vs. anhydrous glasses at low ASI (Fig. 3).

However, there is a complicating factor related to the quench rate. Gupta et al. (1985) found that lower quench rates in hydrous glass favored the formation of BO_4 compared with faster quenching for the same composition, and this effect was also reported by Stebbins and Ellsworth

(1996). There is a strong inherent relationship between the quench rate and water content because adding water strongly decreases melt viscosity and lowers the glass transition temperature (Tg) and the fictive temperature (Tf). For example, the viscosity model for granitic liquids (boron free) as a function of H_2O of Giordano et al. (2008) predicts Tg to be at ca. 950 to 1050 K for a viscosity of 10^{12} Pas. The addition of 4 wt % H_2O will reduce Tg by ca. 300 K. Dingwell et al. (1992) showed that addition of B reduces the viscosity of anhydrous haplogranitic melts. The effect of B is strongly T dependent: at 600 °C, 1 wt % of B_2O_3 will reduce the viscosity by 2 orders of magnitude, whereas at 1000 °C, it will only reduce the viscosity by 0.5 log units. Given the complexity of the structural interplay of B with alkali oxides and alumina, it is not clear how the effect of water addition can be predicted even semi-quantitatively for the compositions investigated in our study. An added complication for our study is that different cooling rates were applied for hydrous vs. anhydrous glasses because the anhydrous melts were produced in open crucibles at ambient pressure and quenched rapidly, while the hydrous melts were synthesized in internally heated pressure vessels and quenching was slower (see methods).

From these considerations, the hydrous glasses will have lower fictive temperatures compared to the anhydrous ones, and the reduced fictive temperature will increase the proportion of BO_4 in the glass. If so, the higher R(IVB) values in hydrous vs. anhydrous samples at low ASI (Fig. 3) may partly reflect the difference in cooling rate, and thus for those compositions, the R(IVB) values of anhydrous glass might better approximate those of the melt.

4.3 Variation in R(IVB) with boron concentration

Schmidt et al. (2004) determined boron coordination in synthetic albite melts ($NaAlSi_3O_8$), with B_2O_3 concentrations ranging from 5 wt % to 17 wt % and H_2O contents of 0 wt % or 4.4 wt %. In all glasses the dominant boron coordination was trigonal. The proportion of tetrahedral boron was 2 % in water-free glasses regardless of the boron concentration, while the addition of water increased the proportion to 6 %, which the authors attributed to the network-modifying effect of OH groups in the melt. Our NMR results for peraluminous glasses show negligible R(IVB) regardless of B_2O_3 variation of 2 wt % to 4 wt %, but the relations for glasses with ASI lower than 1 are more complex. There is a maximum proportion of 90 % R(IVB) in sample J3, duplicated as J11, which has ASI = 0.81 and 0.85 and B_2O_3 = 1.7 and 1.6 wt %, respectively. Raising the boron concentration appears to produce few additional BO_4 groups because the R(IVB) value in sample L2 (5.1 wt % B_2O_3, ASI = 0.85) is 49 % (Table 2). Similarly, the maximum R(IVB) value in metaluminous samples, i.e., ASI near 1, is 54 % (sample K2 with 2.7 wt % B_2O_3 and ASI = 1.1), while its high-boron counterpart concentration (M1: 5.1 wt % B_2O_3, ASI = 1.03) has 20 % R(IVB).

These examples suggest a limited capacity of metaluminous and peralkaline melts to form BO_4 groups, presumably due to a lack of available NBOs. Increasing the boron concentration beyond about 2 wt % B_2O_3 results in a lower relative proportion of tetrahedral boron because the additional boron forms trigonal groups. In samples with ASI > 1.1, the aluminum binds all available alkali elements with NBOs to form AlO_4 groups, and the proportion of BO_4 groups is very low, with the maximum being 7 % (sample P3 with 1.5 wt % B_2O_3).

5 Implications for B-isotope partitioning

Applications of boron isotopes to granitic magma systems depend on knowing how the isotopes fractionate between the melt and other phases, in particular aqueous fluid. This is critical for ore-forming systems, where fluid exsolution from granitic magma is thought to be a key process (e.g., porphyry Cu–Au–Mo deposits, granite and pegmatite Sn–W–Li deposits). The B-isotope composition of tourmaline, which is a common mineral in such deposits, has been used to assess if fluid exsolution took place (Drivenes et al., 2015; Trumbull et al., 2013; Maner and London, 2017; Zhao et al., 2019). However, that assessment depends on knowing the melt–fluid fractionation factor, and existing experimental constraints are conflicting. The studies of Hervig et al. (2002) and Maner and London (2018) predict $\Delta^{11}B_{melt-fluid}$ values of about −7 ‰ at 700 °C, while the combined tourmaline–melt (Cheng et al., 2022) and tourmaline–fluid factors (Meyer et al., 2008) predict less than 1 ‰ difference at 660 °C. Our experimental data on the boron coordination in melts give additional constraints that may help resolve this confusion.

The NMR results show conclusively that boron coordination is dominantly trigonal in all peraluminous glasses examined (ASI > 1.1), regardless of their water and boron concentration. This is in good agreement with the NMR studies of natural peraluminous rhyolite by Tonarini et al. (2002) and Slejko et al. (2007), who reported a maximum R(IVB) proportion of 25 %. Thus, for peraluminous compositions, there should be very little isotopic fractionation between the melt and other phases with trigonal boron coordination, which include aqueous fluid and tourmaline. For tourmaline, this is confirmed by direct tourmaline–melt partitioning data of Cheng et al. (2022), who found $\Delta^{11}B$ values less than 1 ‰ even at the lowest run temperature run of 660 °C. While we find no fault in the studies of Hervig et al. (2002) and Maner and London (2018), the weight of evidence suggests that B-isotope partitioning between peraluminous melt and coexisting aqueous fluid is small.

However, not all granites and rhyolites are peraluminous, and our NMR data predict significant melt–fluid fractionation ($\Delta^{11}B_{melt-fluid}$) for metaluminous and peralkaline melts because of the systematic increase in R(IVB) for glasses with ASI values below 1 (Fig. 3). The exact dependency of

$\Delta^{11}B_{melt-fluid}$ on melt ASI should be the subject of isotope exchange experiments, but an approximation is possible by combining the relationship between ASI and R(IVB) from our study with ab initio calculations of isotope fractionation between trigonal and tetrahedral boron groups in the respective phases. The latter is based on reduced partition functions or β factors as follows (Kowalski and Wunder 2018):

$$\Delta_{melt-fluid} = 1000 \ln \beta \text{ (melt)} - 1000 \ln \beta \text{ (fluid)}. \quad (2)$$

The β factors for $B(OH)_3$ and $B(OH)_4$ in aqueous fluid have been computed as a function of temperature by Kowalski et al. (2013) and Li et al. (2020), while β factors for BO_3 and BO_4 groups in silicate melts at different temperatures were published by Li et al. (2021). Combining these factors results in predicted values of $\Delta^{11}B_{melt-fluid}$ based on Eq. (2). The uncertainty estimates on $\Delta^{11}B$ values calculated in this way are less than 10 ‰ according to Li et al. (2021). The next step is to predict the proportions of trigonal and tetrahedral boron groups in the fluid and melt phases.

For aqueous fluid the proportion of boron complexes $B(OH)_3$ and $B(OH)_4^-$ depends on pH. Studies at low T–p show that the trigonal complex is dominant at neutral and low pH, with equal proportions at pH = 8.6 (Dickson, 1990). Schmidt et al. (2005) determined boron speciation through Raman spectroscopy in aqueous fluid by varying salinity and alkalinity at high pressure and temperature of 2 GPa and 600 °C, respectively. They concluded that trigonal coordination remains dominant over a wide range of p–T–pH conditions typical for crustal rocks, noting that both high salinity and high temperature act to suppress $B(OH)_4$, while high pressure has the opposite effect. Unfortunately, their study could not quantify the ratio of trigonal to tetrahedral species as a function of fluid pH, T, and p, so for a lack of better information, we assume two values for R(IVB) in the fluid phase: 0 % and 30 %. For the melt phase, we calculated β (melt) factors for the full range of R(IVB) from 0 % to 100 % using the BO_3 and BO_4 factors of Li et al. (2021).

The curves in Fig. 6 show the predicted variation in $\Delta^{11}B_{melt-fluid}$ as a function of melt R(IVB) and ASI (lower and upper x axes, respectively). The relation between ASI and R(IVB) was derived from linear regression of the R(IVB) values determined in our experimental glasses (Table 2, Fig. 4) as follows:

$$R(\text{IVB}) = -88.3 \times \text{ASI} + 125.1$$
$$(R^2 = 0.52, \text{ standard error} = 20). \quad (3)$$

The solid and dashed curves in Fig. 6 represent fluid R(IVB) values of 0 % and 30 %, respectively, and the colors represent exemplary temperatures of 527, 727, and 850 °C. This plot can be used to predict the value of $\Delta^{11}B_{melt-fluid}$ for granitic melts as a function of ASI value and temperature. The shift from 0 % to 30 % tetrahedral boron in fluid offsets $\Delta^{11}B_{melt-fluid}$ by 1 ‰ to 3 ‰ depending on temperature.

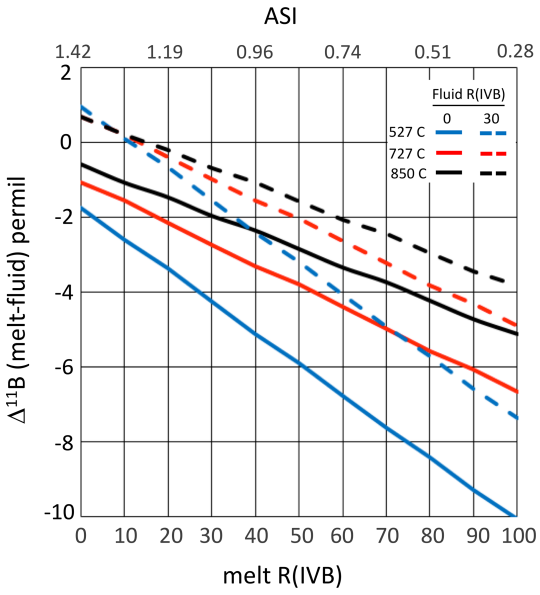

Figure 6. Modeled boron isotope fractionation factors for melt and aqueous fluid ($\Delta^{11}B$) based on combined β factors from Li et al. (2021) for fluid R(IV) of 0 % and 30 % and melt R(IVB) from 0 to 100. The correspondence of ASI values along the top x axis is calculated from R(IVB) according to Eq. (3).

The Macusani rhyolite glass (Pichavant et al., 2024) has ASI = 1.3, and based on our results, the value of R(IVB) should be near 10 %, and $\Delta^{11}B_{melt-fluid}$ at 727 °C (red curve) should be near 0 ‰ to 1 ‰ depending on fluid coordination. In contrast, the experimental melt–fluid fractionation value for Macusani glass reported by Maner and London (2018) is −7.5 ‰ at 750 °C. The authors noted that this strong fractionation implies dominant tetrahedral coordination in the melt, and they wrote that (p. 24) "Spectroscopic studies of these glasses would be the logical next step to quantifying the coordination number of boron oxyanions in hydrous, granitic melt". That step has not been taken for Macusani glass, but Singer et al. (2025) determined the boron coordination by ^{11}B MAS-NMR in synthetic "pegmatite-forming melts", i.e., peraluminous, hydrous granitic melts rich in B, Li, F, and P, and found dominant trigonal coordination. Likewise, our NMR results on haplogranite glasses and the rhyolite studies of Tonarini et al. (2003) and Slejko et al. (2007) indicate that boron in peraluminous melts is mostly in trigonal coordination. For these compositions, then, boron isotope fractionation between melt and aqueous fluid should be small. For other compositions, pending new experimental studies, the relations in Fig. 6 can be used to approximate $\Delta^{11}B_{melt-fluid}$ from the ASI value of the melt.

6 Conclusions

A set of haplogranitic glasses has been synthesized with variable water contents between 0 wt % and 7.2 wt %, ASI values of 0.8 to 1.7, and boron concentrations between 1.5 wt % and 5.2 wt % B_2O_3. The boron coordination in the quenched glasses was analyzed by ^{11}B MAS-NMR.

Boron in all glasses with ASI > 1.1 is nearly completely in trigonal coordination (BO_3 groups) regardless of water content, boron concentration, and ASI value. For other glasses there is a strong negative correlation between ASI and the proportion of tetrahedral boron R(IVB). The maximum value of R(IVB) was 90 % in a glass with ASI = 0.85 wt % and 1.7 wt % B_2O_3. A second-order effect of water on boron coordination was found in samples with low ASI values, suggesting that (OH) in the melt favors the formation of tetrahedral BO_4 groups. However, this effect can also be explained by lower quench rates in the water-rich samples.

Because the boron coordination in melts is a controlling factor in the B-isotope fractionation between melt and a coexisting fluid phase, the results of this study can be applied to boron isotope studies of granitic/rhyolitic systems undergoing fluid exsolution/degassing. For peraluminous compositions with ASI > 1.1, boron is dominantly in trigonal coordination regardless of water content, and isotope fractionation will be minimal, of the order of 1 ‰ at 700 °C. For metaluminous and peralkaline melts, we derived a graphical method to predict $\Delta^{11}B_{melt-fluid}$ from the relationship between melt ASI and R(IVB) established in this study and published ab initio models of boron isotope β factors in silicate melt and aqueous fluid as a function of temperature.

Data availability. The full sets of electron microprobe and Raman spectroscopic data on experimental glasses used in this study are available in the data repository GFZ Data Services (Rauscher et al., 2026).

Author contributions. RBT, BW, SJ, and MW initiated the project. JR synthesized all glass compositions, aided by MJS and JA-SM in the internally heated pressure vessel experiments. JR and FDHW conducted the electron microprobe analyses. MF performed the NMR measurements and supervised their interpretation. DM and MW performed the Raman analyses and interpretation. RBT conceived the paper, MW prepared most figures, and all authors contributed to the interpretation of the results and editing.

Competing interests. At least one of the (co-)authors is a member of the editorial board of *European Journal of Mineralogy*. The peer-review process was guided by an independent editor, and the authors also have no other competing interests to declare.

Disclaimer. Publisher's note: Copernicus Publications remains neutral with regard to jurisdictional claims made in the text, published maps, institutional affiliations, or any other geographical representation in this paper. The authors bear the ultimate responsibility for providing appropriate place names. Views expressed in the text are those of the authors and do not necessarily reflect the views of the publisher.

Acknowledgements. Funding for this study was provided by the Deutsche Forschungsgemeinschaft (DFG) under the framework of Priority Programme SPP 2238 (DOME). The paper was greatly improved after constructive comments and suggestions by Nagia S. Tagiara, the anonymous reviewer, and associate editor Didier Laporte.

Financial support. This research has been supported by the Deutsche Forschungsgemeinschaft (grant nos. TR 256/8-1, JA 1469/12-1, WU 752/2-1, WI 2000/24-1, HO1337/49-1, and MI3189/1-1).

The article processing charges for this open-access publication were covered by the GFZ Helmholtz Centre for Geosciences.

Review statement. This paper was edited by Didier Laporte and reviewed by Nagia S. Tagiara and one anonymous referee.

References

Acosta-Vigil, A., London, D., Morgan VI, G. B., and Dewers, T. A.: Solubility of excess alumina in hydrous granitic melts in equilibrium with peraluminous minerals at 700–800 °C and 200 MPa, and applications of the aluminum saturation index, Contrib. Mineral. Petrol., 146, 100–119, https://doi.org/10.1007/s00410-003-0486-6, 2003.

Aldermann, O. L. G., Tagiara, N. S., Slagle, I., Gabrielsson, R. M., Boggs, P., Wagner, M., Rossini, A., John, S., Rocha, L., Wilson, R. M., Hawbaker, J., Martin, S. W., Hannon, A. C., Kamitsos, E. I., and Feller, S. A.: A review of the fraction of four-coordinated boron in binary borate glasses and melts, Rep. Prog. Phys., 88, 076501, https://doi.org/10.1088/1361-6633/adc69c, 2025

Barton, M. D.: Granitic magmatism and metallogeny of southwestern North America, Trans. R. Soc. Edin., 87, 261–280, https://doi.org/10.1017/S0263593300006672, 1996.

Bray, P. J.: Nuclear magnetic resonance studies of glass structure, J. Non-cryst. Solids, 73, 19–45, https://doi.org/10.1016/0022-3093(85)90335-7, 1985.

Bray, P. J. and O'Keefe, J. G.: Nuclear magnetic resonance investigations of the structure of alkali borate glasses, Phys. Chem. Glass., 4, 37–46, 1963.

Cheng, L., Zhang ,C., Zhou, Y., Horn, I., Weyer, S., and Holtz, F.: Experiments reveal enrichment of ^{11}B in granitic melt resulting from tourmaline crystallization, Geochem. Persp. Lett., 20, 37–42, https://doi.org/10.7185/geochemlet.2206, 2022.

Codeço, M. S., Weis, P., Trumbull, R. B., Pinto, F., and Lecumberri-Sanchez, P.: Chemical and boron isotopic composition of hydrothermal tourmaline from the Panasqueira W-Sn-Cu deposit, Portugal, Chem. Geol., 468, 1–16, https://doi.org/10.1016/j.chemgeo.2017.07.011, 2017.

Cuney, M.: Felsic magmatism and uranium deposits, Bull. Soc. Geol. France, 185, 75–92, https://doi.org/10.2113/gssgfbull.185.2.75, 2014.

De la Cruz, E., Mueller, A., Trumbull, R. B., Faria, P., Andersen, T., Erambert, M., and Kristoffersen, M.: Boron sources of tourmaline-rich Nb-Y-F-pegmatites in south Norway: implications for pegmatite melt origin, Prec. Res., 410, 107474, https://doi.org/10.1016/j.precamres.2024.107474, 2024.

Dickson, A. G.: Thermodynamics of the dissociation of boric acid in synthetic seawater from 273.15 to 318.15 K, Deep-Sea Res., 37, 755–766, https://doi.org./10.1016/0198-0149(90)90004-F, 1990.

Dingwell, D. B., Knoche, R., Webb, S. L., and Pichavant, M.: The effect of B2O3 on the viscosity of haplogranitic liquids, Am. Mineral., 77, 457–461, 1992.

Dingwell, D. B., Pichavant, M., and Holtz, F.: Experimental studies of boron in granitic melts, Rev. Miner. Geochem., 33, 331–386, ISBN13 978-0-939950-41-6, 2002

Driveness, K., Larsen, R. B., Mueller, A., Sørensen, B. E., Wiedenbeck, M., and Raanes, M. P.: Late-magmatic immiscibility during batholith formation: assessment of B isotopes and trace elements in tourmaline from the Land's End granite, SW England, Contrib. Mineral. Petrol., 169, 56, https://doi.org/10.1007/s00410-015-1151-6, 2015.

Filip, J., Bosi, F., Novák, M., Skogby, H., Tuček, J., Čuda, J., and Wildner, M.: Iron redox reactions in the tourmaline structure: High-temperature treatment of Fe^{3+}-rich schorl, Geochim. Cosmochim. Acta, 86, 239–256, https://doi.org/10.1016/j.gca.2012.02.031, 2012.

Giordano, D., Russell, J. K., and Dingwell, D. D: Viscosity of magmatic liquids: a model, Earth Planet. Sc. Lett., 271, 123–134, https://doi.org/10.1016/j.epsl.2008.03.038, 2008.

Gupta, P. K., Lui, M. L., and Bray, P. J.: Boron coordination in rapidly cooled and in annealed aluminum borosilicate glass fibers, J. Am. Ceram. Soc., 68, C82, https://doi.org/10.1111/j.1151-2916.1985.tb09639.x, 1985.

Hervig, R. L., Moore, G. M., Williams, L. B., Peacock, S. M., Holloway, J. R., and Roggensack, K.: Isotopic and elemental partitioning of boron between hydrous fluid and silicate melt, Am. Mineral., 87, 769–774, https://doi.org/10.2138/am-2002-5-620, 2002.

Hess, K. U., Dingwell, D. B., and Webb, S. L.: The influence of excess alkalis on the viscosity of a haplogranitic melt, Am. Mineral., 80, 297–304, https://doi.org/10.2138/am-1995-3-411, 1995.

Holtz, F., Dingwell, D. B., and Behrens, H.: Effects of F, B_2O_3 and P_2O_5 on the solubility of water in haplogranite melts compared to natural silicate melts, Contrib. Mineral. Petrol., 113, 492–501, https://doi.org/10.1007/BF00698318, 1993.

Kowalski, P. M. and Wunder, B.: Boron isotope fractionation among vapor-liquid-solids-melts: experiments and atomistic modeling, in: Boron Isotopes – The Fifth Element, Advances in Isotope Geochemistry, Vol. 7, edited by: Marschall, H. R. and Foster, G. L., Springer, Berlin-Heidelberg, 33–69, https://doi.org/10.1007/978-3-319-64666-4, 2018.

Kowalski, P. M., Wunder, B., and Jahn, S.: Ab initio prediction of equilibrium boron isotope fractionation between minerals and aqueous fluids at high P and T, Geochim. Cosmochim. Acta, 101, 285–301, https://doi.org/10.1016/j.gca.2012.10.007, 2013.

Lehmann, B., Dietrich, A., Heinhorst, J., Métrich, N., Mosbah, M., Palacios, C., Schneider, H.-J., Wallianos, A., Webster, J., and Winkelmann, L.: Boron in the Bolivian Tin belt, Mineral. Dep., 35, 223–232, https://doi.org/10.1007/s001260050017, 2000.

Lehmann, B.: Formation of tin ore deposits: A reassessment, Lithos, 402/403, 105756, https://doi.org/10.1016/j.lithos.2020.105756, 2021.

Li, Y.-C., Chen, H.-W., Wei, H. Z., Jiang, S. Y., Palmer, M. R., Van De Ven, T. G. M., Hohl, S., Lu, J. J., and Ma, J.: Exploration of driving mechanisms of equilibrium boron isotope fractionation in tourmaline group minerals and fluid: a density functional theory study, Chem. Geol., 536, 119466, https://doi.org/10.1016/j.chemgeo.2020.119466, 2020.

Li,Y.-C., Wei, H. Z., Palmer, M. R., Jiang, S. Y., Liu, X., Williams-Jones, A. E., Ma, J., Lu, J. J., Lin, Y. B., and Dong, G.: Boron coordination and B/Si ordering controls over equilibrium boron isotope fractionation among minerals, melts, and fluids, Chem. Geol., 561, 120030, https://doi.org/10.1016/j.chemgeo.2020.120030, 2021.

London, D.: Experimental synthesis and stability of tourmaline: a historical overview, Can. Mineral., 49, 117–136, https://doi.org/10.3749/canmin.49.1.117, 2011.

London, D., Morgan, G. B., and Wolf, M. B.: Boron in granitic rocks and their contact aureoles, Rev. Mineral. Geochem., 33, 299–330, ISBN13 978-0-939950-41-6, 2002.

Maner IV, J. L. and London, D.: The boron isotopic evolution of the Little Three pegmatites, Ramona, CA, Chem. Geol., 460, 70–83, https://doi.org/10.1016/j.chemgeo.2017.04.016, 2017.

Maner IV, J. L., and London, D.: Fractionation of the isotopes of boron between granitic melt and aqueous solution at 700 °C and 800 °C (200 MPa), Chem. Geol., 489, 16–27, https://doi.org/10.1016/j.chemgeo.2018.05.007, 2018.

Marschall, H. R. and Foster, G. L. (Eds.): Boron Isotopes – The Fifth Element, Advances in Isotope Geochemistry, Vol. 7, Springer, Berlin-Heidelberg, 289 pp., https://doi.org/10.1007/978-3-319-64666-4, 2018.

Massiot, D., Fayon, F., Capron, M., King, I., Le Calvé, S., Alonso, B., Durand, J.-O., Bujoli, B., Gan, Z., and Hoatson, G.: Modelling one- and two-dimensional solid-state NMR spectra, Mag. Res. Chem., 40, 70–76, https://doi.org/10.1002/mrc.984, 2002.

Meyer, C., Wunder, B., Meixner, A., Romer, R. L., and Heinrich, W.: Boron-isotope fractionation between tourmaline and fluid: an experimental re-investigation, Contrib. Mineral. Petrol., 156, 259–267, https://doi.org/10.1007/s00410-008-0285-1, 2008.

Morgan VI, G. B. and London, D.:. Effect of current density on the electron microprobe analysis of alkali aluminosilicate glasses, Am. Mineral., 90, 1131–1138, https://doi.org/10.2138/am.2005.1769, 2005.

Navrotsky, A.: Thermochemistry of borosilicate melts and glasses, from Pyrex to pegmatites, Rev. Mineral. Geochem., 33, 165–180, ISBN13 978-0-939950-41-6, 2002.

Pichavant, M., Erdmann, S,. Kontak, D. J., Michaud, J. A-S., and Villaros, A.: Trace element partitioning in strongly peraluminous rare-metal silicic magmas – Implications for fractionation processes and for the origin of the Macusani Vol-

canics (SE Peru), Geochim. Cosmochim. Acta, 365, 229–252, https://doi.org/10.1016/j.gca.2023.11.021, 2024.

Rauscher, J. Michaud J. A.-S., Mothan, D., Sieber, M. J., Trumbull, R. B., Wilke, F. D. H., Wilke, M., and Wunder, B.: Chemical composition of synthetic boron-rich haplogranite glasses from electron microprobe and confocal Raman spectroscopic analyses, GFZ Data Services, https://doi.org/10.5880/fidgeo.d.2026.001, 2026.

Romer, R. L. and Kroner, U.: Sediment and weathering control on the distribution of Paleozoic magmatic tin-tungsten mineralization, Mineral. Depos., 50, 327–338, https://doi.org/10.1007/s00126-014-0540-5, 2016.

Schmidt, B. C.: Effect of boron on the water speciation in (alumino)silicate melts and glasses, Geochim. Cosmochim. Acta, 68, 5013–5025, https://doi.org/10.1016/j.gca.2004.06.036, 2004.

Schmidt, B. C., Zotov, N., and Dupree, R.: Structural implications of water and boron dissolution in albite glass, J. Non-crystal. Solids, 37, 207–219, https://doi.org/10.1016/j.jnoncrysol.2004.04.007, 2004.

Schmidt, C., Thomas, R., and Heinrich, W.: Boron speciation in aqueous fluids at 22 to 600 °C and 0.1 MPa to 2 GPa, Geochim. Cosmochim. Acta, 69, 275–281, https://https://doi.org/10.1016/j.gca.2004.06.018, 2005.

Schmitt, A. K. and Simon, J. I.: Boron isotopic variations in hydrous rhyolitic melts: a case study from Long Valley, California, Contrib. Mineral. Petrol., 146, 590–605, https://doi.org/10.1007/s00410-003-0514-6, 2004.

Schiavi, F., Bolfan-Casanova, N., Withers, A. C., Médard, E., Laumonier, M., Laporte, D., Flaherty, T., and Gómez-Ulla, A.: Water quantification in silicate glasses by raman spectroscopy: correcting for the effects of confocality, density and ferric ion, Chem. Geol., 483, 312–331, https://doi.org/10.1016/j.chemgeo.2018.02.036, 2018.

Scholze, H.: Glas: Natur, Stuktur und Eigenschaften, Springer, Berlin, 339 pp., ISBN 3540084037, https://doi.org/10.1007/978-3-662-07495-4, 1988.

Schulze, F., Behrens, H., Holtz, F., Roux, J., and Johannes, W.: The influence of H_20 on the viscosity of a haplogranitic melt, Am. Mineral., 81, 1155–1165, https://doi.org/10.2138/am-1996-9-1014, 1996.

Singer, C. R., Behrens, J., Horn, I., Fechtelkord, M., and Weyer, S.: Boron diffusion, related isotope fractionation and the structural role of B in pegmatite forming melts, Geochim. Cosmochim. Acta, 392, 70–87, https://doi.org/10.1016/j.gca.2024.11.023, 2025.

Slejko, F. F., Petrini, R., and Pizzanelli, S.: The characterization of boron sites in the glass structure of a calc-alkaline magma (Capraia Island, Italy), Period. Mineral., 76, 3–9, http://hdl.handle.net/11568/113202 (last access: 10 August 2025), 2007.

Smith, M. P. and Yardley, B. W. D.: The boron isotopic composition of tourmaline as a guide to fluid processes in the southwestern England orefield: an ion microprobe study, Geochim. Cosmochim. Acta, 60, 1415–1427, https://doi.org/10.1016/0016-7037(96)00007-5, 1996.

Spallanzani, R., Koga, K. T., Cichy, S. B., Wiedenbeck, M., Schmidt, B. C., Oelze, M., and Wilke, M.: Lithium and Boron diffusivity and isotopic fractionation in hydrated rhyolitic melts, Contrib. Mineral. Petrol., 177, 74, https://doi.org/10.1007/s00410-022-01937-2, 2022.

Stebbins, J. F. and Ellsworth, S. E.: Temperature effects on structure and dynamics in borate and borosilicate liquids: high-resolution and high-temperature NMR results, J. Am. Ceram. Soc., 79, 2247–2256, https://doi.org/10.1111/j.1151-2916.1996.tb08969.x, 1996.

Sun, W., Zhao, Z., Mo, X., Dong, G., Li, X., Yuan, W., Wang, T., Wang, B., Pan, T., Han, J., Zheng, F., and Tang, Y.: Tourmaline as an indicator for pegmatite evolution and exploration: A case study from the Chakabeishan deposit, northeastern Tibetan Plateau, Ore Geol. Rev., 165, 105892, https://doi.org/10.1016/j.oregeorev.2024.105892, 2024.

Sunde, Ø., Friis, H., Andersen, T., Trumbull, R. B., Wiedenbeck, M., Lyckberg, P., Agostini, S., Casey, H., and Yu, P.: Boron isotope composition of coexisting tourmaline and hambergite in alkaline and granitic pegmatites, Lithos, 352/353, 105293, https://doi.org/10.1016/j.lithos.2019.105293, 2020.

Thomas, R., Foerster, H. J., and Heinrich, W.: The behavior of boron in a peraluminous granite-pegmatite system and associated hydrothermal solutions: a melt and fluid-inclusion study, Contrib. Mineral. Petrol., 144, 457–472, https://doi.org/10.1007/s00410-002-0410-5, 2003.

Tonarini, S., Forte, C., Petrini, R., and Ferrara, G.: Melt/biotite $^{11}B/^{10}B$ isotopic fractionation and the boron local environment in the structure of volcanic glasses, Geochim. Cosmochim. Acta, 67, 1863–1873, https://doi.org/10.1016/S0016-7037(02)00987-0, 2003.

Trumbull, R. B. and Slack, J. F.: Boron isotopes in the continental crust: granites, pegmatites, felsic volcanic rocks, and related ore deposits, in: Boron Isotopes – The Fifth Element, Advances in Isotope Geochemistry, Vol. 7, edited by: Marschall, H. R. and Foster, G. L., Springer, Berlin-Heidelberg, 249–272, https://doi.org/10.1007/978-3-319-64666-4, 2018.

Trumbull, R. B., Beurlen, H., Wiedenbeck, M., and Soares, D. R.: The diversity of B-isotope variations in tourmaline from rare-element pegmatites in the Borborema Province of Brazil, Chem. Geol., 352, 47–62, https://doi.org/10.1016/j.chemgeo.2013.05.021, 2013.

Trumbull, R. B., Codeço, M.S., Jiang, S. Y., Palmer, M. R., and Slack, J. F.: Application of boron isotopes in tourmaline to understanding hydrothermal ore systems, Ore Geol. Rev., 125, 103682, https://doi.org/10.1016/j.oregeorev.2020.103682, 2020.

Wilke, F. D. H.: Appearance, study and a possible correction for boron: a phenomenon in ultra-soft X-ray measurements using a synthetic multilayer crystal and the EPMA, Eur. J. Mineral., 35, 59–64, https://doi.org/10.5194/ejm-35-59-2023, 2023.

Wolf, M. and London, D.: Boron in granitic magmas: stability of tourmaline in equilibrium with biotite and cordierite, Contrib. Mineral. Petrol., 130, 12–30, https://doi.org/10.1007/s004100050346, 1997.

Wu, J. and Stebbins, J. F.: Quench rate and temperature effects on boron coordination in aluminoborosilicate melts, J. Non-cryst. Solids, 356, 2097–2108, https://doi.org/10.1016/j.jnoncrysol.2010.08.015, 2010.

Wu, J., Potuzak, M., and Stebbins, J. F.: High-temperature in situ ^{11}B NMR study of network dynamics in boron-containing glass-forming liquids, J. Non-cryst. Solids, 357, 3944–3951, https://doi.org/10.1016/j.jnoncrysol.2011.08.013, 2011.

Zajacz, Z., Halter, W. E., Pettke, T., and Guillong, M.: Determination of fluid/melt partition coefficients by LA-ICPMS analysis

of co-existing fluid and silicate melt inclusions: Controls on element partitioning, Geochim. Cosmochim. Acta, 72, 2169–2197, https://doi.org/10.1016/j.gca.2008.01.034, 2008.

Zhao, H. D., Zhao, K. D., Palmer, M. R., and Jiang, S. Y.: In-situ elemental and boron isotopic variations of tourmaline from the Sanfang granite, South China: Insights into magmatic-hydrothermal evolution, Chem. Geol., 504, 190–204, https://doi.org/10.1016/j.chemgeo.2018.11.013, 2019.

Zhao, Z., Yang, X., Zhang, T., Lu, Y., Li, W., and Zhang, Z.: Geochemical characteristics and boron isotopes of tourmaline from the Baishaziling tin deposit, Nanling Range: Constraints on magmatic-hydrothermal processes, Ore Geol. Rev., 142, 104695, https://doi.org/10.1016/j.oregeorev.2022.104695, 2022.